

Project Report for 250A and 250B: Kinetic particle simulations
in plasmas in a global toroidal geometry

Sadhitro De

Project supervisor: Dr. Animesh Kuley

Department of Physics
Indian Institute of Science
Bangalore - 560012, India.

Abstract

The gyrokinetic toroidal code (GTC) has been upgraded for global simulations by coupling the core and scrape-off layer (SOL) regions across the magnetic separatrix. The ability of the improved code in constructing field-aligned grids, regardless of the geometry of the tokamak, is showcased through the creation of such grids using the realistic equilibrium data from DIII-D and EAST tokamaks. A fully kinetic particle pusher for high frequency waves (ion cyclotron frequency and beyond) and, a guiding center pusher for low frequency waves have been implemented using cylindrical coordinates in a global toroidal geometry. The two integrators correctly capture the particle orbits and agree well with each other, conserving energy and canonical angular momentum. Finally, as a further verification of the capability of the new code, self-consistent simulations of zonal flows in the core region of the DIII-D tokamak were carried out.

Contents

1	Introduction	5
2	Equilibrium quantities	8
3	Field-aligned grids construction	8
4	Particle dynamics	10
5	Self-consistent simulations	15
5.1	Boundary conditions	15
5.2	Zonal flow verification	16
6	Discussions	18
	Appendix	20
(A)	1D and 2D spline interpolation	20
(B)	Boris-push scheme	22
(C)	Results from the EAST tokamak	24
	References	27

List of Figures

1	A typical poloidal cross section of a tokamak having a single divertor. <i>Picture courtesy: Google Images.</i>	6
2	(a) Poloidal current function $F(\psi)$ in $m-T$ on uniform flux grid, and (b) poloidal flux function in web/rad on rectangular (R, Z) grid points for DIII-D shot #158103 at 3050 ms. The magnitude of the flux function is indicated by the colours. The last closed flux surface and the limiter points are represented by the black and magenta lines, respectively.	9
3	Components of magnetic field (a) B_Z , (b) B_R , and (c) B_ζ for DIII-D shot #158103 at 3050 ms. The magnitude of the magnetic field components are indicated by colours. The last closed flux surface and the limiter points are represented by the black and magenta lines, respectively.	9
4	GTC-X computational grids on a poloidal plane coupling core and SOL. Field aligned mesh at the core, separatrix, SOL, and private regions are represented by red, black, magenta, and green, respectively. Fully kinetic (blue and green) and guiding center (magenta and yellow) calculations of trapped particle orbits in the core (51.66 keV) and cross separatrix (59.42 keV). Limiter points are represented by the dark brown line.	12

5	Variation of the toroidal angle ζ with time for the trapped particle orbits of Fig. 4, in the core (blue) and the cross-separatrix (red) regions. The oscillations of ζ indicate the bounce motion and the gradual change in the mean level of the oscillations implies the toroidal precession of these bounce orbits.	13
6	Time step convergence of the fully kinetic Boris integrator. (a) and (c) represent the relative energy error (in the range of floating point cutoff error) and, (b) and (d) show the relative canonical angular momentum error for the core and cross-separatrix regions, respectively.	14
7	Time step convergence of the guiding center second order Runge Kutta integrator.. (a) and (c) represent the relative energy error and, (b) and (d) show the relative canonical angular momentum error for the core and cross-separatrix regions, respectively.	14
8	Time step convergence of guiding center pusher for a boundary particle that is brought back into the simulation domain after leaving it. The figure on top shows the relative error in total energy while, the one below represents the relative error in the canonical angular momentum.	16
9	Time series plot of the normalized zonal electric field on a given flux surface. Here, R_0 is the major radius of the DIII-D tokamak and c_s is the ion sound speed.	18
10	Velocity rotation scheme of Boris. The velocities are shown as projections of the total velocities onto the plane perpendicular to \mathbf{B} (which is assumed to be pointing into the plane). <i>Picture courtesy: Reference [7]</i>	23
11	Poloidal current function in $m - T$ on uniform flux (left), and poloidal flux function in web/rad on rectangular (R, Z) (right) for the EAST tokamak. The magnitude of the flux function is indicated by the colours. The last closed flux surface and the limiter points are represented by the magenta and red lines, respectively.	24
12	Contour plots of the components of the magnetic field, B_Z (left) B_R (middle) and B_ζ (right), for EAST tokamak. The magnitude of the magnetic field components are indicated by colours. The last closed flux surface and the limiter points are represented by the magenta and red lines, respectively.	25
13	Field-aligned grids for the EAST tokamak. The grids in the core are shown in blue, those on the separatrix surface in red and those in the SOL region in violet. The limiter surface is drawn in red.	25
14	FK (blue) and GC(yellow) orbits of (a) a passing ion, (b) a trapped ion and (c) a cross-separatrix ion in the geometry of the EAST tokamak. The magnitude of the poloidal flux is represented by colours. The last closed flux surface and the limiter surface are shown in magenta and red respectively.	26

1 Introduction

Tokamaks are toroidally shaped devices that are used in the confinement of plasmas at high temperatures and densities with the goal of producing huge amounts of clean energy through sustained fusion reactions. The confinement is mainly brought about by crossed toroidal and poloidal magnetic fields. This constrains the ions in the plasma to gyrate about and translate along the field lines, thus preventing them from colliding with the walls as a result of their random thermal velocities. The overall magnetic field used in plasma confinement is predominantly toroidal. As a result, the gradient of this field mainly points toward the centre of the torus. Hence, the inner walls of the tokamak experience a large magnetic force due to this gradient, also known as the “grad-B force”. This resulted in a tremendous pressure on the inner walls of earlier tokamaks which had circular cross sections. Modern tokamaks have a D-shaped cross section, where the flat side of the D lies on the inside of the torus. This evens out the force acting on different portions of the inner wall, thereby reducing the pressure on it. As a result of the D-shape, the ions drift away from the field lines (the drift also occurs due to the curvature of the magnetic field itself and also due to the $E \times B$ force). Due to this drift, the plasma can collide with the walls of the device and cause sputtering to occur. This would not only damage the walls, but the ablated material sputtered from the walls (mainly comprising of heavy metals) would absorb heat from the plasma, cooling it down and hindering fusion. In order to prevent damage to the walls, a limiter (a covering made of a light material) was introduced. The limiter projects into the plasma from the inner walls of the torus, as a result of which the plasma collides with the limiter instead, preventing the walls from being damaged. However, the problem sputtering from the limiter and production of fusion ash (heavier ions produced as a result of fusion which remained within the fuel in the tokamak) still persisted. A solution in this regard was the introduction of divertor plates. The divertor plates changed the geometry of the plasma within the torus. It divided the cross section of the torus into two regions - the core, having closed field lines, and the scrape-off layer (SOL) consisting of open field lines, separated by a magnetic separatrix which happens to be the last closed flux surface of the core region. There is also another region, known as the private region, lying below the magnetic separatrix in Fig. 1. The separatrix between the private and SOL regions and that between the core and the SOL touch at a given point, known as the X-point. At the X-point, the magnetic flux goes to zero. The presence of the divertor elongates the plasma, bringing it away from the walls. More importantly, it shapes the field lines such that the heavier ablated impurities and the fusion ash descend downwards due to their weight, follow the field lines along the separatrix and escape out of the plasma through the divertor plates. This significantly improves the sustainability of the plasma at high temperatures. Modern day tokamaks have either one (eg: ITER, France; DIII-D, U.S.A.) or two (eg: EAST, China) divertors.

One of the important challenges in achieving a viable operating regime for ITER and future fusion reactors is associated with the nonlinear turbulent dynamics of the plasma in the SOL [1]. The plasma

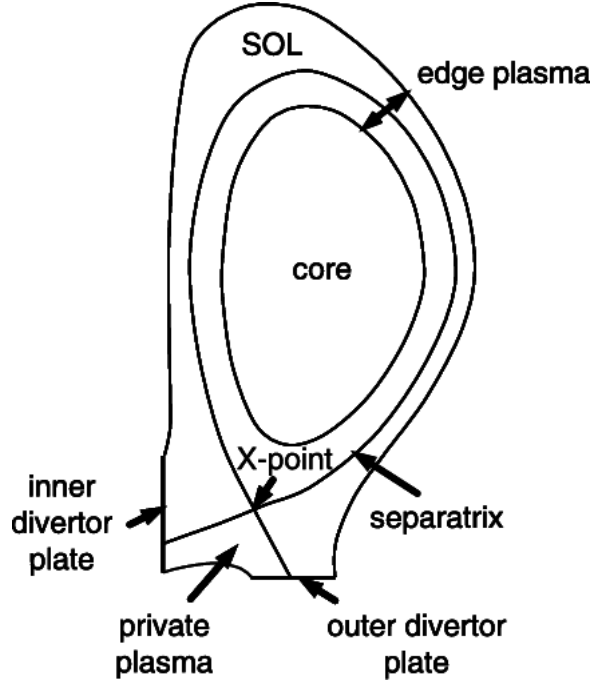


Figure 1: A typical poloidal cross section of a tokamak having a single divertor. *Picture courtesy: Google Images.*

characteristics in SOL can greatly affect the overall confinement properties of the device, regulate the heat load to the tokamak wall and, influence the level of fusion ash, the impurity dynamics and plasma shaping effects. Furthermore, the SOL dynamics can play a significant role in the radio-frequency heating of the plasma, since the radio waves that are sent in for heating the plasma first interacts with the plasma in the SOL. A thorough understanding of the plasma dynamics in the SOL remains an outstanding open problem. It is challenging, mainly due to the multiple spatial and temporal scales associated with different instabilities in that region.

Though there have been fluid simulation codes that have tried to simulate the SOL dynamics, their results have shown quite a few discrepancies with the experimental findings. These were attributed to the fact that kinetic effects could be significant in some SOL processes such as ion orbit losses, X-point losses and plasma sheath dynamics to name a few. Hence, the need of the hour is a kinetic approach that can couple the different geometries of the core and SOL regions across the magnetic separatrix. Such a study will provide helpful insights into the dynamics of the plasma in the SOL, which will be of utmost importance in the design of present and future fusion reactors.

A significant advancement in this regard was the development of a kinetic code, the gyrokinetic toroidal code (GTC) [2], which has been successful in studying turbulence and transport properties in the core. The GTC is a well-benchmarked code based on first principles. It however uses conventional magnetic coordinates wherein the equations of motion encounter a singularity of the metric at the magnetic separatrix. This is mainly due to the vanishing of the poloidal magnetic field at the X-point(s). As a result, it is unable to couple the core and SOL regions. Moreover, the poloidal angle suffers a

discontinuity across the separatrix.

Here, we report a significant enhancement that we have made over the GTC by the use of a cylindrical coordinate system (R, Z, ζ) . R is the radial coordinate in the toroidal plane, Z represents the direction perpendicular to the toroidal plane and ζ is the toroidal angle. The new coordinate system overcomes all the aforementioned difficulties face by GTC, leading us to name our code as GTC-X (X standing for the X-point, since the new code does not suffer from the singularity at the X-point unlike GTC). The use of a cylindrical coordinate system for the advancement of the particle dynamics, which allows particle motion in arbitrarily shaped flux surfaces including the magnetic separatrix and the X-point(s), which GTC could not have done.

In the new code, we have developed a method of field-aligned particle-grid interpolations using an axisymmetric mesh in the cylindrical coordinates. The grids can be built as per the resolution requirements of the simulation. These field-aligned particle-grid interpolations can achieve the same order of numerical efficiency as the field-aligned mesh in magnetic flux coordinates, used earlier in GTC [3]. We have also developed a fully kinetic (FK) particle pusher to capture the effect of high frequency waves (ion cyclotron frequency and beyond) and a guiding center (GC) pusher to describe the particle dynamics associated with low frequency waves (\ll ion cyclotron frequency). As a testimony to the capability of GTC-X to reproduce the existing physical phenomena, we carried out self-consistent simulations of zonal flows in the core region. The collisionless damping of the zonal electric field to a non-zero steady-state value, verifies the famous theory of Rosenbluth and Hinton on the collisionless damping of zonal flows [4].

As a note I would like to add that, we have worked with experimental equilibrium data generated by the discharges of the DIII-D tokamak of the United States and the EAST tokamak of China. In the majority of the report I have outlined the results we obtained using the data from DIII-D. Some of the DIII-D results such as reading of the equilibrium parameters, field calculation, grids construction and some of the work on particle pushers was done before I started the project. I modified parts of the particle pusher and completed the remainder of it so that it could be used in self-consistent simulations. I also did half the diagnosis of the pushers (the entire diagnosis of the GC pusher). The entire portion on self-consistent simulations and their diagnostics was done by me. As a verification of the applicability of the code to the equilibrium profile of any geometry of any device, I studied the equilibrium data of the EAST tokamak (which has two divertor plates), calculated the magnetic fields, constructed the grids and observed different kinds of particle orbits (both FK and GC) in this new geometry. The results of the EAST device and the modifications that were required in the code for studying the new geometry have been mentioned in Appendix C.

2 Equilibrium quantities

The data file obtained from the DIII-D discharge (plasma shot #158103 at 3050 ms) gave the profiles of a number of equilibrium quantities including the safety factor, poloidal current function $F(\psi)$ and poloidal flux function ψ over a rectangular grid of points on a poloidal cross-section of the tokamak (see Fig. 2). All these quantities were read using a numerical interface. Being an axisymmetric system, the components of the magnetic field (B_R , B_Z , B_ζ) can be written in terms of $F(\psi)$ and the derivatives of ψ as follows:

$$B_R = -\frac{1}{R} \frac{\partial \psi}{\partial Z}, \quad B_Z = \frac{1}{R} \frac{\partial \psi}{\partial R}, \quad B_\zeta = \frac{F(\psi)}{R} \quad (1)$$

The discharge data file gave the equilibrium quantities over a coarse mesh of points. However, the micro-scale turbulence demands much denser grid points in R and Z directions. Therefore, it is necessary to map the coarse equilibrium mesh to a dense computational mesh, in order to attain sufficient numerical accuracy. This was achieved by constructing 1D and 2D spline representations of $F(\psi)$ and ψ respectively [3] over the rectangular grid representing a poloidal cross-section of the tokamak (see Appendix A). The spline representations enabled accurate interpolation of the respective quantities and also allowed accurate calculations of their derivatives. Using the 2D spline representation of ψ we calculated the equilibrium magnetic field components (using Eqn. (1)) and the results are shown in Fig. 3. After that 2D spline representations of the magnetic field components were also calculated since these would later be required in the grid constructions over the flux surfaces and in the particle integrators for finding the magnetic field at the particle position.

3 Field-aligned grids construction

Construction of field-aligned grids aids in the particle-grid interpolations in three dimensions during the self-consistent simulations, since particles travel along the magnetic field lines. Equi-spaced grids in the radial component R were constructed along the outer mid-plane ($Z = 0$) of the poloidal cross-section. Using these values of R as the reference, we constructed flux surfaces (through spline interpolations of the equilibrium data) which were equi-spaced in R along the outer mid-plane.

The final grids were constructed by tracing out the magnetic field lines in the poloidal direction along the afore-constructed flux surfaces. This was done with the help of the following equations:

$$\frac{dR}{dS} = b_R = \frac{B_R}{B_p}, \quad \frac{dZ}{dS} = b_Z = \frac{B_Z}{B_p} \quad (2)$$

where $B_p = \sqrt{B_R^2 + B_Z^2}$ is the magnitude of the poloidal magnetic field and S is an increment along the field line. Choosing S to be very small, the increments in R and Z were calculated as the field lines were traced out poloidally. In this way, we constructed the field aligned grids in the cylindrical coordinates

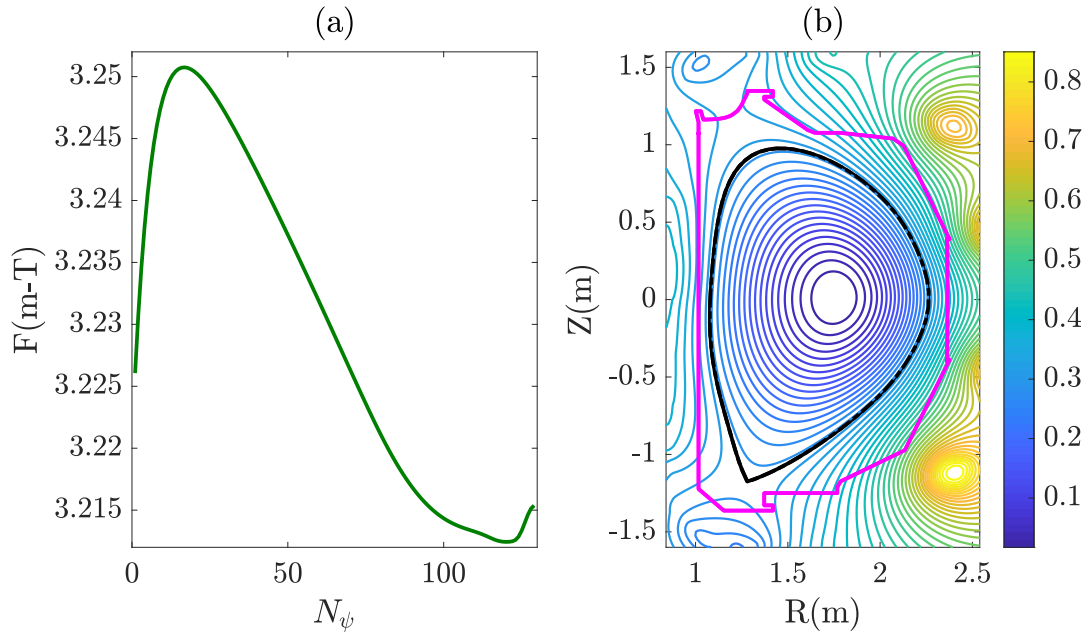


Figure 2: (a) Poloidal current function $F(\psi)$ in $m - T$ on uniform flux grid, and (b) poloidal flux function in web/rad on rectangular (R, Z) grid points for DIII-D shot #158103 at 3050 ms. The magnitude of the flux function is indicated by the colours. The last closed flux surface and the limiter points are represented by the black and magenta lines, respectively.

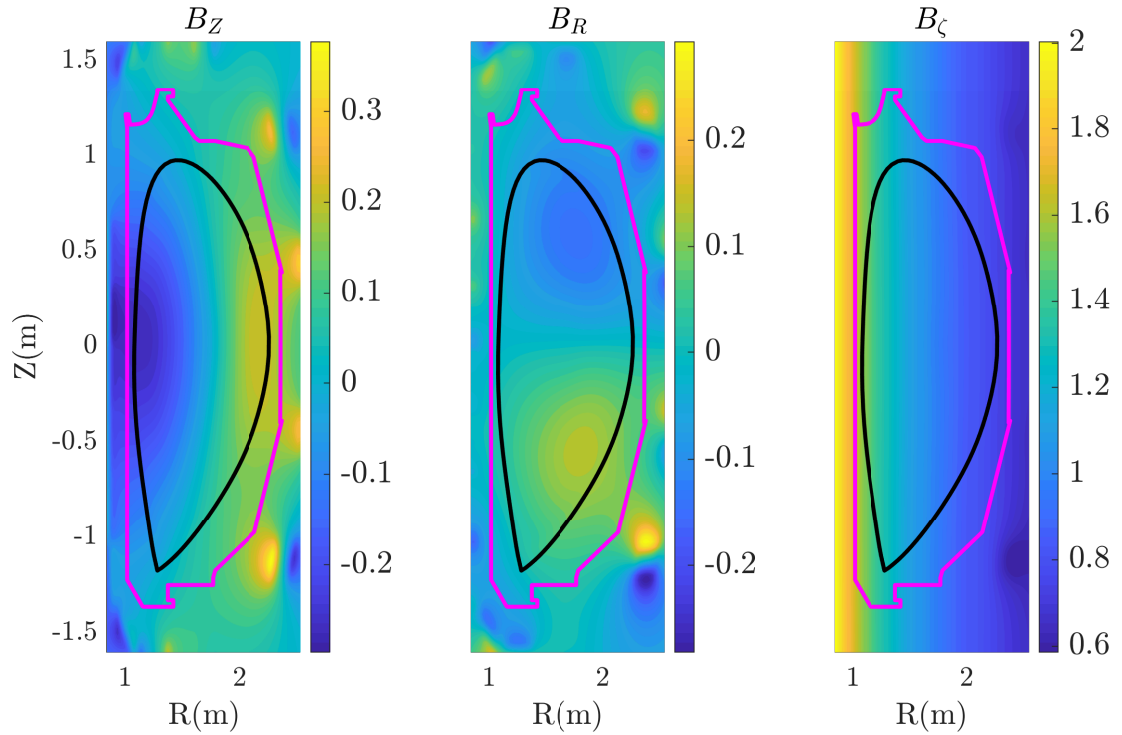


Figure 3: Components of magnetic field (a) B_Z , (b) B_R , and (c) B_ζ for DIII-D shot #158103 at 3050 ms. The magnitude of the magnetic field components are indicated by colours. The last closed flux surface and the limiter points are represented by the black and magenta lines, respectively.

(R, Z) , the results of which (for the DIII-D tokamak) are shown in Fig. 4 in the next section. In the SOL region, consisting of open field lines, the grids were constrained to lie within the confines of the tokamak using a ray-casting algorithm [5]. A similar but slightly more complicated construction was carried out for the EAST tokamak of China which has two divertors as opposed to the single divertor of the DIII-D tokamak (see Appendix C).

4 Particle dynamics

The efficiency of particle simulation strongly depends on the advancement of the dynamical quantities. In GTC-X we have developed particle pushers for both fully kinetic particles as well as guiding center particles using cylindrical coordinates (R, ζ, Z) in a global toroidal geometry. In fully kinetic dynamics (FK), the full motion of the particle (translation + gyration about the field lines) is studied and is necessary in the investigation of high frequency phenomena. In guiding center (GC) dynamics, only the translatory motion of the centre of gyration of the particle is studied and is mainly helpful in the investigation of low frequency phenomena (\ll ion gyration frequency). The formalism behind the two particle pushers/integrators and their implementation are described as follows.

Fully kinetic particle dynamics is described by the six dimensional Vlasov equation

$$\left[\frac{\partial}{\partial t} + \mathbf{v} \cdot \nabla + \frac{q}{m} (\mathbf{E} + \mathbf{v} \times \mathbf{B}) \cdot \frac{\partial}{\partial \mathbf{v}} \right] f_{FK} = 0 \quad (3)$$

where f_{FK} is the fully kinetic particle distribution function, q is the particle charge, and m is the particle mass. The above equation governs the evolution of f_{FK} in the fully kinetic approach. The time evolution of the phase space coordinates of a single particle, in the presence of a self-consistent electromagnetic field, is governed by the Lorentz-force equation as follows:

$$\frac{d\mathbf{r}}{dt} = \mathbf{v} \quad \frac{d\mathbf{v}}{dt} = \frac{q}{m} (\mathbf{E} + \mathbf{v} \times \mathbf{B}) \quad (4)$$

The two constants of motion of single-particle motion are the total energy ϵ and toroidal angular momentum p_ζ [6] which, in cylindrical coordinates, are defined as follows:

$$\epsilon = \frac{m}{2} (v_R^2 + R^2 v_\zeta^2 + v_z^2)$$

$$p_\zeta = mR^2 v_\zeta + q\psi_p$$

where ψ_p is the poloidal flux at the position of the particle.

For numerical evaluation of the FK particle trajectories, a standard leapfrog method is used wherein, the time-centred velocity is evolved from time $t - \Delta t/2$ to $t + \Delta t/2$ while the particle position is made

to evolve from t to $t + \Delta t$ using the time-centred velocities. This method provides a second order accuracy while requiring a single force or field evaluation per step thus allowing a quicker and more accurate simulation of the particle trajectories. The evolution of time-centred velocities was carried out with the help of the Boris-push algorithm – a widely used particle-integrator scheme in standard PIC (particle-in-cell) simulations of plasmas [7] (see Appendix B).

The guiding centre dynamics are described by the following equation in the four-dimensional GC phase space:

$$\left[\frac{\partial}{\partial t} + \mathbf{X} \cdot \nabla + \dot{v}_{\parallel} \frac{\partial}{\partial v_{\parallel}} \right] f_{GC} = 0 \quad (5)$$

where f_{GC} is the GC distribution function, \mathbf{X} is the GC position and v_{\parallel} is the GC velocity parallel to the magnetic field. The evolution of the GC distribution function can be described by the following equations of GC motion [8]:

$$\dot{\mathbf{X}} = \frac{\mathbf{B}^*}{B_{\parallel}^*} v_{\parallel} + \mathbf{v}_E + \mathbf{v}_g + \mathbf{v}_c \quad (6)$$

$$\dot{v}_{\parallel} = -\frac{1}{m} \frac{\mathbf{B}^*}{B_{\parallel}^*} (\mu \nabla B + q \nabla \phi) \quad (7)$$

where $\mathbf{B}^* = \mathbf{B} + (Bv_{\parallel}/\omega_c) \nabla \times \hat{b}$ is the modified magnetic field, $\mu = mv_{\perp}^2/2B$ is the magnetic moment, $B_{\parallel}^* = \mathbf{B}^* \cdot \hat{b}$ and ω_c is the ion cyclotron frequency. The $E \times B$ drift velocity \mathbf{v}_E , curvature drift \mathbf{v}_c and the grad-B drift \mathbf{v}_g are given as follows:

$$\mathbf{v}_E = \frac{c\mathbf{B} \times \nabla \phi}{BB_{\parallel}^*}$$

$$\mathbf{v}_c = \frac{B}{B_{\parallel}^*} \frac{v_{\parallel}^2}{\omega_c} \nabla \times \hat{b}$$

$$\mathbf{v}_g = \frac{\mu}{m\omega_c} \frac{\mathbf{B} \times \nabla B}{B_{\parallel}^*}$$

Here too, the constants of motion are the total energy ϵ and the toroidal angular momentum p_{ζ} .

$$\epsilon = \frac{mv_{\parallel}^2}{2} + \mu B$$

$$p_{\zeta} = mRv_{\parallel}(B_{\zeta}/B) + q\psi_p$$

The equations of motion (Eqns. (6) and (7)) are evaluated in the cylindrical coordinates to obtain v_R , v_{ζ} , v_{\parallel} and the time derivative of v_{\parallel} . Using these, the GC position \mathbf{X} is updated using a 2nd order RK integrator.

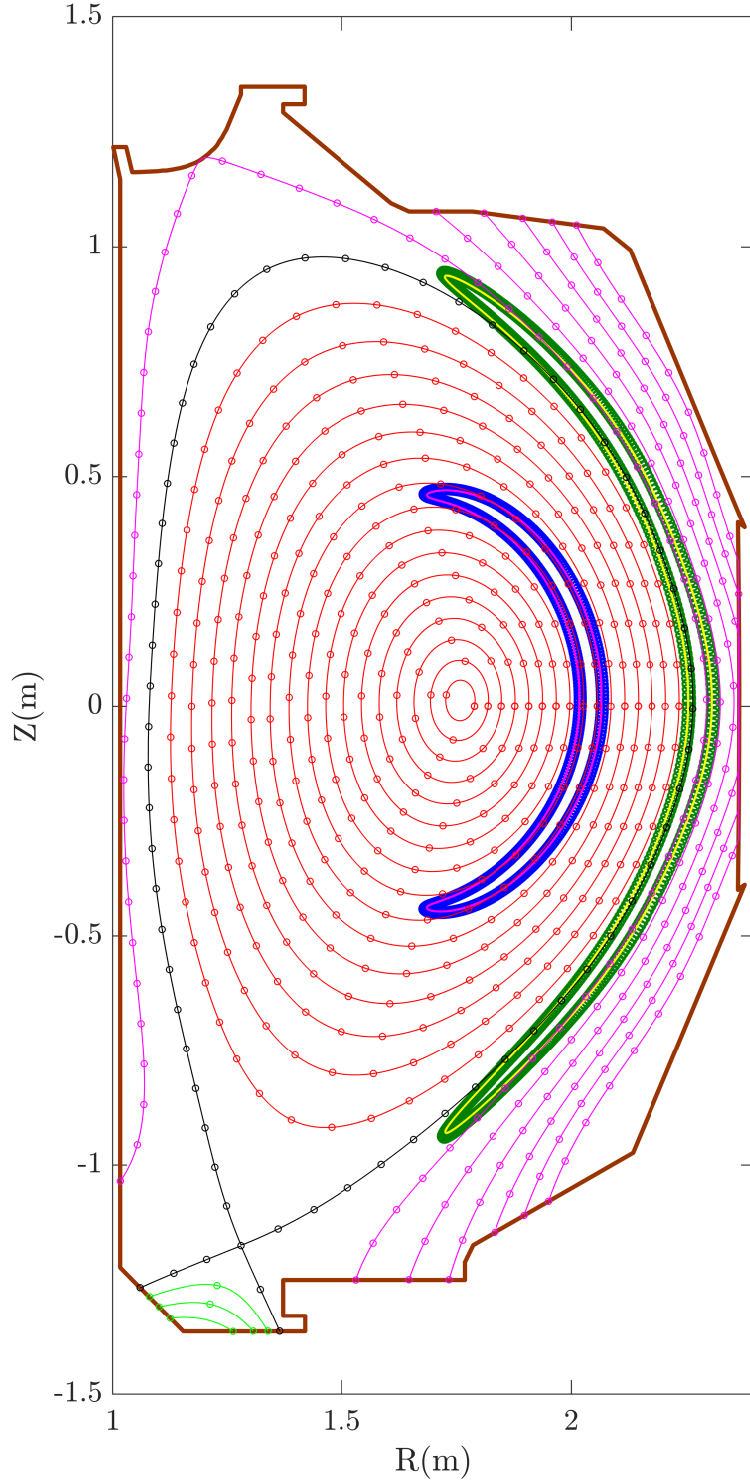


Figure 4: GTC-X computational grids on a poloidal plane coupling core and SOL. Field aligned mesh at the core, separatrix, SOL, and private regions are represented by red, black, magenta, and green, respectively. Fully kinetic (blue and green) and guiding center (magenta and yellow) calculations of trapped particle orbits in the core (51.66 keV) and cross separatrix (59.42 keV). Limiter points are represented by the dark brown line.

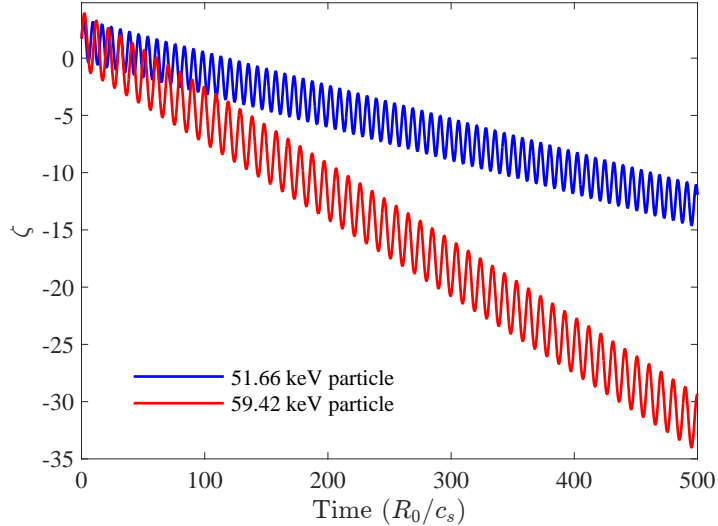


Figure 5: Variation of the toroidal angle ζ with time for the trapped particle orbits of Fig. 4, in the core (blue) and the cross-separatrix (red) regions. The oscillations of ζ indicate the bounce motion and the gradual change in the mean level of the oscillations implies the toroidal precession of these bounce orbits.

Parameter	Core	Cross-separatrix
R/R_0	1.154	1.289
Z/R_0	0.0	0.0
ζ	1.570	1.570
$v_R/\omega_c R_0$	3.371×10^{-3}	3.371×10^{-3}
$v_Z/\omega_c R_0$	5.371×10^{-3}	5.371×10^{-3}
v_ζ/ω_c	1.271×10^{-3}	1.271×10^{-3}

Table 1: Initial conditions of the FK particle pusher. R_0 is the value of R at the magnetic axis.

Parameter	Core	Cross-separatrix
R/R_0	1.147	1.281
Z/R_0	0.0	0.0
ζ	1.570	1.570
$v_{\parallel}/\omega_c R_0$	2.547×10^{-3}	3.017×10^{-3}
$\sqrt{\mu B_0}/\omega_c R_0$	4.545×10^{-3}	4.642×10^{-3}
v_ζ/ω_c	1.271×10^{-3}	1.271×10^{-3}

Table 2: Initial conditions of the GC particle pusher. B_0 is the value of B at the magnetic axis.

Poloidal projections of the FK and GC orbits of trapped particles in the core and the cross-separatrix regions are shown in Fig. 4. These orbits were obtained by loading a single particle into the code with different initial positions and velocities, and then evolving their trajectories according to the numerical schemes mentioned above. The initial conditions for the different orbits have been tabulated in Tables 1 and 2. The trapped particles perform a so-called bounce motion as they bounce back and forth between two points along the field lines within the tokamak, thereby giving a banana-like shape to the poloidal projections of their orbits. The trapping of particles occurs due to the parallel (toroidal) component of the of the grad-B force $\mathbf{F} = -\mu \nabla B$ which slows down/speeds up the motion of the particles in the

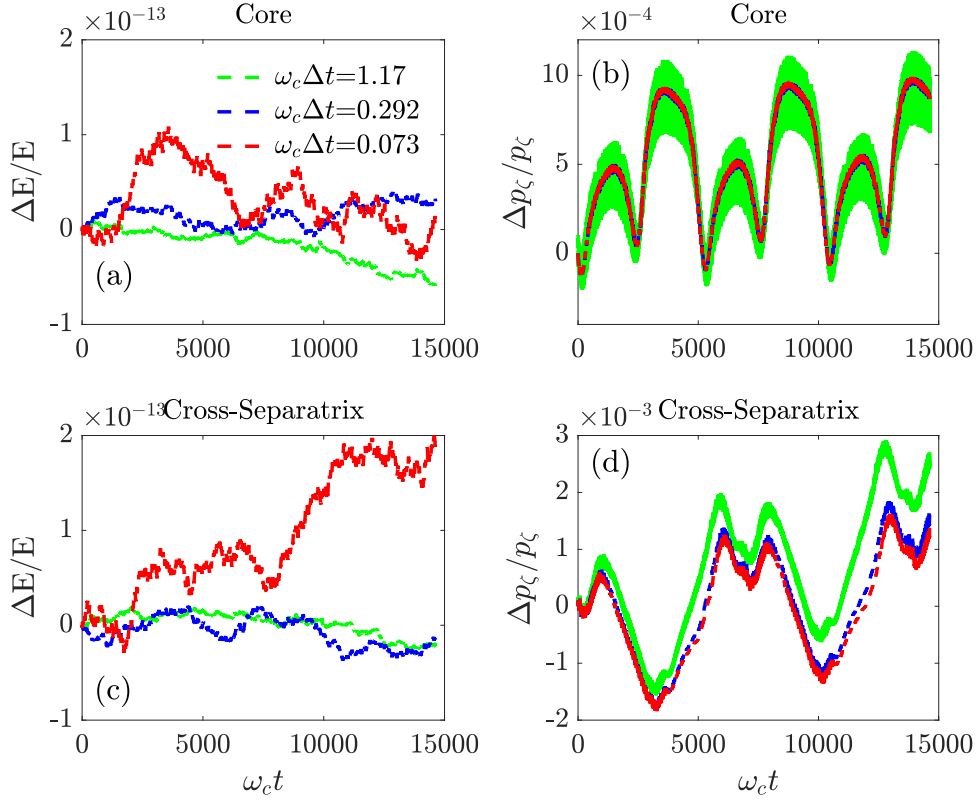


Figure 6: Time step convergence of the fully kinetic Boris integrator. (a) and (c) represent the relative energy error (in the range of floating point cutoff error) and, (b) and (d) show the relative canonical angular momentum error for the core and cross-separatrix regions, respectively.

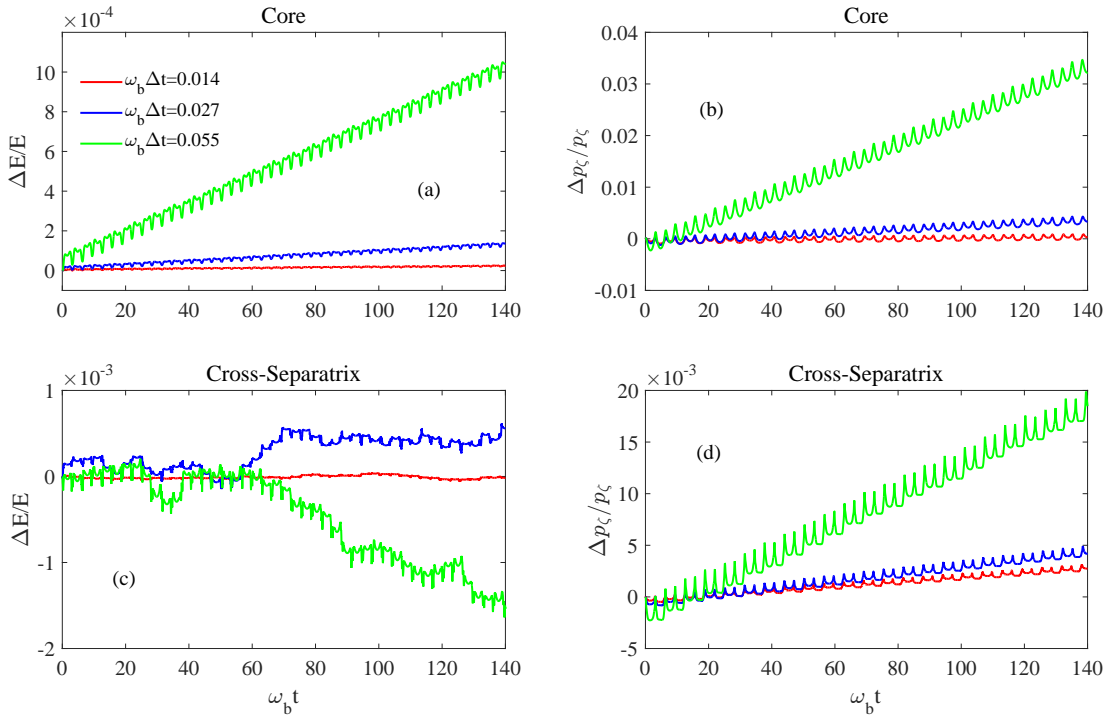


Figure 7: Time step convergence of the guiding center second order Runge Kutta integrator.. (a) and (c) represent the relative energy error and, (b) and (d) show the relative canonical angular momentum error for the core and cross-separatrix regions, respectively.

toroidal direction. As a result, particles with lower toroidal velocity are more likely to be trapped. These trapped particle orbits also precess along the torus of the tokamak, the evidence of which is shown in the variation of the toroidal position of the particle with time in Fig. 5.

As a check of our numerical schemes, we plotted the time variation of the errors in the conserved quantities for both the FK and GC cases considering trapped particle in the core and the cross-separatrix regions (i.e. using the same initial conditions that were used for Fig. 4 for the respective orbits). The results are shown in Figs. 6 and 7 wherein ω_b represents the bounce frequency (i.e. frequency of the bounce motion of the trapped particles) and ω_c is the ion cyclotron frequency as mentioned before. From these magnitude of the errors shown in these plots for different values of the time step Δt , one can infer the superiority of the Boris-push scheme used in the FK simulations over the 2nd order RK method used for the GC simulations.

5 Self-consistent simulations

Self-consistent guiding center simulations were carried out in order to verify the physical properties of zonal flows, which are explained later.

5.1 Boundary conditions

It is computationally very expensive to simulate the entire volume of the tokamak all at once, since accurate simulations require closely spaced grids and ample number of particles per grid area, both of which will be too large to be handled by the limited computational resources. As a result, we generally choose to simulate a certain volume of the tokamak bounded between two flux surfaces. As the particles move around, some of them happen to leave the domain of simulation. This destroys the quasineutrality (charge-neutral nature) of the plasma. In order to prevent this, the escaping particles should be brought back into the simulation domain by some means. In our code, we have implemented the following procedure in bringing back the escaping particles.

We first found the flux at the position of the particle at a given instant of time $\psi_p(t)$, the simulation domain being the interval (ψ_1, ψ_2) , and the poloidal angle at that instant $\theta_p(t)$. If $\psi_p(t) < \psi_1$ or $\psi_p(t) > \psi_2$ i.e. if the particle lay outside the simulation domain, we re-initialized ψ_p with its value at the earlier time step when the particle was within the simulation domain (i.e. $\psi_p(t) = \psi_p(t - \Delta t)$) and θ_p was re-initialized as $\theta_p(t) = 2\pi - \theta_p(t - \Delta t)$. This technique preserves the nature of the motion of trapped particles at the domain boundaries. Knowing $\psi_p(t)$ and $\theta_p(t)$, we obtained the new coordinates (R_p, Z_p) of the guiding center by finding expressions for R and Z in terms of ψ and θ . This was done by constructing 2D splines for $R = R(\psi, \theta)$ and $Z = Z(\psi, \theta)$ in the same way as mentioned in Appendix A. The velocity of the escaping particle is re-initialized with its value at the previous time step when the

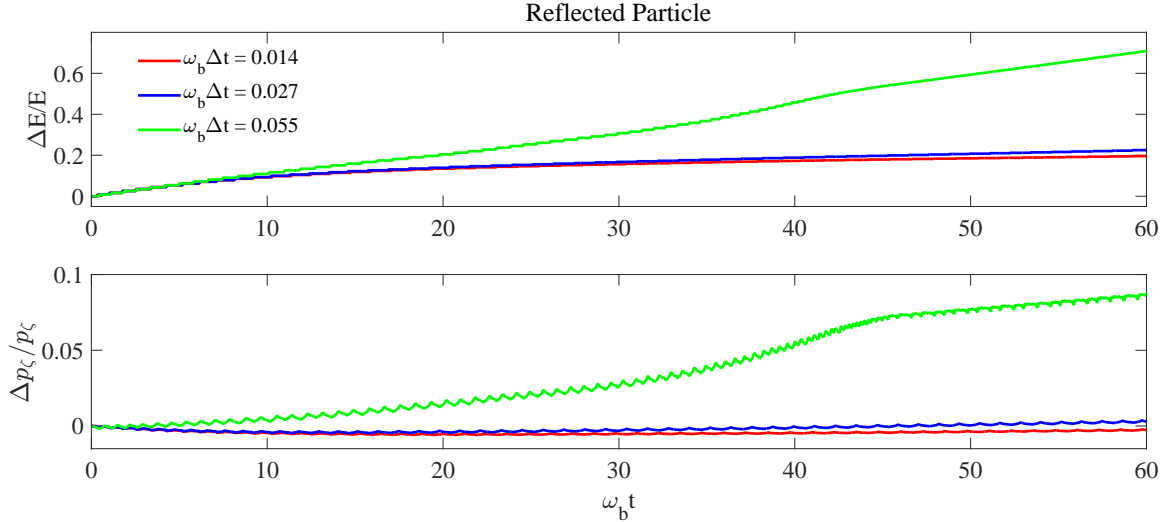


Figure 8: Time step convergence of guiding center pusher for a boundary particle that is brought back into the simulation domain after leaving it. The figure on top shows the relative error in total energy while, the one below represents the relative error in the canonical angular momentum.

particle lay within the simulation domain. This was done to ensure the conservation of the total energy and the toroidal angular momentum.

In order to test the above technique, we applied it to the cross-separatrix particle in Fig. 4, using the separatrix as the boundary of our simulation domain such that the particle was brought back every time it crossed the separatrix. The relative error in the total energy and the canonical angular momentum for different time-steps is shown in Fig. 8. We observe that the conservation of the invariants is better at the smaller time-step sizes ($\omega_b \Delta t = 0.014, 0.027$) than that at a bigger time-step size ($\omega_b \Delta t = 0.055$). However, the overall extent of conservation is not as good as observed earlier, in the absence of a domain boundary. This is because the boundary condition used here is not a perfect one. It however gave us good results in the self-consistent simulations of large number of particles over a long time intervals, as we would observe later in the verification of zonal flows in the core region.

5.2 Zonal flow verification

Zonal flows are low frequency electrostatic modes that are spontaneously generated by turbulence and, in turn, regulate the level of turbulence. They play an important role in transport process in a plasma. They are driven by drift-wave instabilities (which can even be of the form of a small perturbation of the density of the plasma). In the absence of instabilities in a collisionless plasma, these flows are damped by wave-particle interactions (Landau damping). Rosenbluth and Hinton [4] analytically showed that zonal flows, in the absence of collisions, damp out to a non-zero residual level instead of vanishing completely, due to a neoclassical polarization shielding caused by the finite width of banana orbits of the trapped particles. In this section, we demonstrate the collisionless damping of zonal flows and verify the Rosenbluth-Hinton theory by observing the variation of the zonal electric field $E(\psi)$, at a given point in

the core region, with respect to time.

In order to simulate these zonal flows, we solve the flux-surface-averaged gyrokinetic Poisson's equation [3] at every time step.

$$\langle \nabla_{\perp}^2 \phi \rangle = \left\langle \left(\frac{T_i}{Z_i^2 n_i} \nabla_{\perp}^2 - \frac{T_i}{\rho_i^2 Z_i^2 n_i} \right) \frac{1}{e} (Z_i n_i - n_e) \right\rangle \quad (8)$$

Here $\langle \dots \rangle$ implies flux-surface average. T_i , n_i and Z_i are the temperature, density and atomic number of the ion species respectively. e is the unit electronic charge and n_e is the electron density. ρ_i is the ion gyroradius. Since we are dealing with zonal quantities, we are only concerned with the component of the Laplacian perpendicular to the flux surfaces. As shown in Xiao et al. [3], the flux-surface-averaged Laplacian can be written in the magnetic flux coordinates (ψ, θ, ζ) as

$$\langle \nabla_{\perp}^2 \phi \rangle = \frac{1}{J_0(\psi)} \left[\frac{\partial}{\partial \psi} \left(J_0(\psi) \langle g^{\psi\psi} \rangle \frac{\partial \langle \phi \rangle}{\partial \psi} \right) \right] \quad (9)$$

where $J_0(\psi)$ is the flux-surface averaged Jacobian. In writing Eqn. (9) we have neglected the higher order toroidal coupling terms by assuming a small inverse aspect-ratio. In our simulations we load a uniform ion temperature and density profile. As a result, T_i and n_i are constant all throughout the simulation domain. Integrating Eqn. (8) once with respect to ψ , we obtain the zonal electric field as follows:

$$E(\psi) = \frac{\partial \langle \phi \rangle}{\partial \psi} = \frac{T_i}{n_i Z_i^2 e^2} \frac{\partial \langle \rho_c \rangle}{\partial \psi} - \frac{1}{\langle g^{\psi\psi} \rangle J_0(\psi)} \int \frac{T_i}{n_i Z_i^2 e^2} \left\langle \frac{1}{\rho_i^2} \right\rangle \langle \rho_c \rangle J_0(\psi) d\psi \quad (10)$$

Here $\langle \rho_c \rangle = e(Z_i \langle \bar{n}_i \rangle - \langle n_e \rangle)$ is the flux-averaged total charge density. \bar{n}_i is the ion guiding center density. Solving Eqn. (10) at every time step, we have incorporated the field information in our GC pusher which updates the particle position accordingly. However, Eqn. (10) gives the zonal electric as a function of ψ while the guiding center equations of motion in cylindrical coordinates require the R and Z components of the zonal field. Hence we simply do a coordinate transformation to obtain E_R and E_Z i.e. $E_R = (\partial\psi/\partial R)E_{\psi}$ and $E_Z = (\partial\psi/\partial Z)E_{\psi}$, where $E_{\psi} = E(\psi)$. In our simulation of zonal flows, we started off by loading the particles (here, thermal ions) in a certain domain within the core region such that, they are uniformly distributed between any two consecutive flux surfaces. For this, we had to calculate the volume associated with each flux surface. We began by taking an approximation of the volume associated with each grid cell and then added them up over the respective flux surfaces to get the flux surface volumes. After that we loaded the particles accordingly and calculated the number of particles lying within a certain neighborhood of each flux surface (i.e. their weights associated with a given flux surface), thereby obtaining the flux surface volumes in terms of the number of particles. The newly calculated flux surface volumes would also serve as the flux-averaged Jacobian $J_0(\psi)$ at each flux surface. As the system evolves with time, the particles leaving the simulation domain are brought

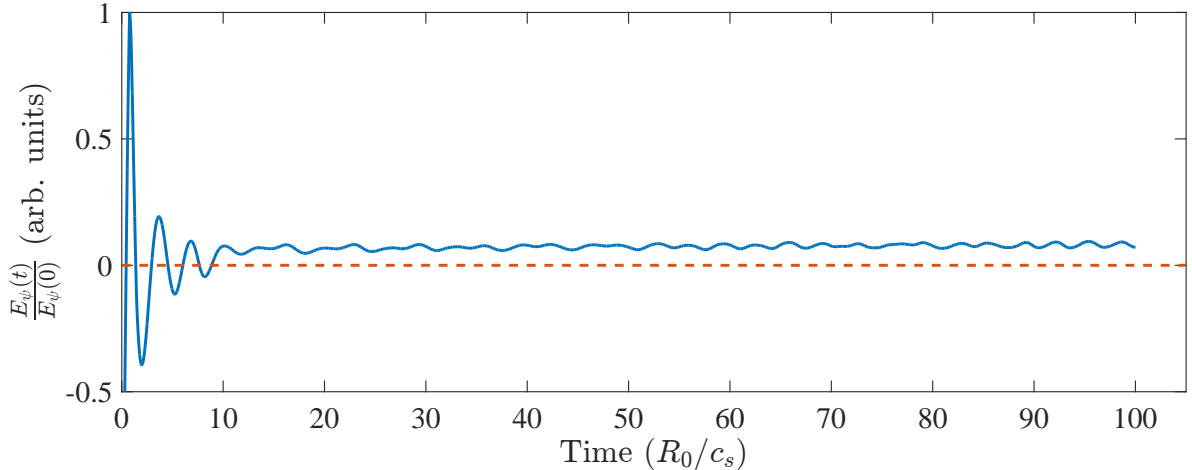


Figure 9: Time series plot of the normalized zonal electric field on a given flux surface. Here, R_0 is the major radius of the DIII-D tokamak and c_s is the ion sound speed.

back using the boundary conditions discussed earlier, in order to maintain quasi-neutrality and energy conservation. Full-f ions and adiabatic electrons were used in the present study of zonal flows. The initial velocities of the particles followed a Maxwellian distribution. The simulation domain extended from $\psi_1 = 0.4\psi_{sep}$ to $\psi_2 = 0.9\psi_{sep}$ and the domain-width along the outer midplane was $\Delta \approx 68.02\rho_i$.

The zonal flows were initiated by driving the system for a certain duration of time with a low magnitude electric field having a sinusoidal dependence on ψ . After switching off the external perturbation (i.e. the driving field) the system was allowed to evolve self-consistently with time. Fig. 9 shows the time evolution of the zonal field E_ψ on removing the external perturbation after a small duration of time. Finally E_ψ settles down to a non-zero residual value, in the absence of collisions. This non-zero value is the Rosenbluth-Hinton residual level and is of great importance in determining the level of turbulence in the plasma.

6 Discussions

In conclusion, we have developed, to an extent, a robust code GTC-X for simulating the plasma dynamics in both the core and SOL regions. GTC-X is shown to be capable of coupling the two regions of different geometries since it uses cylindrical coordinates which overcome the difficulty faced by the traditional magnetic coordinates at the magnetic separatrix surface. Further, the use of a kinetic approach enables us to take into account certain important features that are neglected in the fluid approach. In our code, we have developed a suitable interface for reading the equilibrium file generated from any tokamak. The code is also capable of constructing field-aligned grids in any possible geometry. We have successfully formulated and implemented particle integrators for both fully kinetic and guiding centre motions in cylindrical coordinates. Finally we have been able to carry out self-consistent simulations through im-

plementation of suitable boundary conditions, 3D particle-grid interpolations and a 1D Poisson's equation solver. This enabled us to verify the physics of zonal flows in the core region, thereby benchmarking GTC-X as a viable operational code that can be used for large scale simulations of tokamak plasmas.

In future, we seek to extend our code to verify of other kinds of plasma waves and instabilities in the core and SOL. This will give us a deeper insight into the dynamics of the SOL region, thereby allowing us to overcome the problems associated with radio-frequency heating and plasma losses near the walls of the tokamak.

Appendix

(A) 1D and 2D spline interpolation

For a 1D function $f(x)$ the following 1D B-spline representation can be used:

$$f(x) = f(1, i) + f(2, i)h + f(3, i)h^2 \quad (11)$$

where $x_i \leq x < x_{i+1}$, $h = x_{i+1} - x_i$, $i = 0, 1, \dots, N$ and $f(1, i) = f(x_i)$. We assume a uniform grid size in x . The spline coefficients $f(2, i)$ and $f(3, i)$ are related to the first and second order differentials in x and can be calculated from $f(1, i)$ using a finite difference method on a spline grid. Using the conditions of continuity of the function $f(x)$ and its first derivative,

$$f(x_i + h) = f(x_{i+1}), \quad f'(x_i + h) = f'(x_{i+1})$$

we find that

$$f(1, i + 1) = f(1, i) + f(2, i)h + f(3, i)h^2 \quad (12)$$

$$f(2, i + 1) = f(2, i) + 2hf(3, i) \quad (13)$$

The above equations can be used iteratively to obtain $f(2, i)$ and $f(3, i)$. The two initial values $f(2, 1)$ and $f(3, 1)$ remain to be determined. These depend on the features of the 1D function $f(x)$ close to the initial point x_0 . As $x \rightarrow x_0$, the following three relevant cases need to be considered:

(i) $f(x) = a + b\Delta x$ where $\Delta x = x - x_0$. Then the coefficients are

$$f(3, 1) = 0 \quad (14)$$

and

$$f(2, 1) = [f(1, 2) - f(1, 1)]/h \quad (15)$$

(ii) $f(x) = a + b(\Delta x)^2$. Then the coefficients are found to be

$$f(2, 1) = 0 \quad (16)$$

and

$$f(3, 1) = [f(1, 2) - f(1, 1)]/h^2 \quad (17)$$

(iii) $f(x) = a + b\Delta x + c(\Delta x)^2$. The coefficients are found to be

$$f(2, 1) = [4f(1, 2) - f(1, 3) - 3f(1, 1)] / (2h) \quad (18)$$

and

$$f(3, 1) = [f(1, 2) - f(1, 1) - f(2, 1)h] / h^2 \quad (19)$$

In our simulations we assumed the behaviour of the 1D functions, close to the initial point, to be of the form given in case (iii). Hence the initial spline coefficients in our constructions were given by Eqns. (18) and (19). The iteration equations then take the form

$$f(2, i) = -f(2, i-1) + 2[f(1, i) - f(1, i-1)] / h \quad (20)$$

$$f(1, i+1) = hf(2, i)/2 + f(1, i+2)/4 + 3f(1, i)/4 \quad (21)$$

$$f(3, i) = [f(2, i+1) - f(2, i)] / (2h) \quad (22)$$

Eqn. (21) is needed to smooth out $f(1, i)$ while Eqns. (20) and (22) can be directly obtained using Eqns. (12) and (13). The end point is taken care of as follows:

$$f(2, N) = -f(2, N-1) + 2[f(1, N) - f(1, N-1)] / h \quad (23)$$

$$f(3, N) = 0 \quad (24)$$

After constructing the 1D B-splines, we can also obtain the derivative of the function $f(x)$ within the domain of interpolation.

$$f'(x) = f(2, i) + 2hf(3, i) \quad (25)$$

All the 1D derivatives of the equilibrium quantities were calculated using Eqn. (25).

After constructing the 1D B-splines, one can easily obtain the B-spline representations of 2D functions of the form $f(x, y) = \sum_n g_n(x)h_n(y)$, where each of the functions $g_n(x)$ and $h_n(y)$ can be represented by 1D B-splines of the form $g_n(x) = g_n(1, i) + g_n(i, 2)\Delta x + g_n(i, 3)(\Delta x)^2$ and $h_n(y) = h_n(1, i) + h_n(i, 2)\Delta y + h_n(i, 3)(\Delta y)^2$ respectively. Most the 2D equilibrium quantities can be written in the form of $f(x, y)$. The 2D spline representation of $f(x, y)$ can then be written as

$$\begin{aligned} f(x, y) = & f(1, i, j) + f(2, i, j)\Delta x + f(3, i, j)(\Delta x)^2 + f(4, i, j)\Delta y + f(5, i, j)\Delta y\Delta x + f(6, i, j)\Delta y(\Delta x)^2 \\ & + f(7, i, j)(\Delta y)^2 + f(8, i, j)(\Delta y)^2\Delta x + f(9, i, j)(\Delta y\Delta x)^2 \end{aligned} \quad (26)$$

where the coefficients $f(m, i, j)$, $m = 1, \dots, 9$ can be related to the spline coefficients of the 1D splines of g_n and h_n . Since the equilibrium poloidal flux ψ was given to us over grids that were equi-spaced in R and Z , we could directly construct a 2D spline representation of ψ using the above procedure. This representation also allowed us to find the coordinates (R, Z) of the particle as functions of ψ and θ during the self-consistent simulations.

The partial derivatives of the spline representation $f(x, y)$ over a uniform grid of points are found as

$$\begin{aligned} f_x(x, y) &= f(2, i, j) + f(5, i, j)\Delta y + f(8, i, j)(\Delta y)^2 \\ &+ 2\Delta x [f(3, i, j) + f(6, i, j)\Delta y + f(9, i, j)(\Delta y)^2] \end{aligned} \quad (27)$$

$$\begin{aligned} f_y(x, y) &= f(4, i, j) + f(5, i, j)\Delta x + f(6, i, j)(\Delta x)^2 \\ &+ 2\Delta y [f(7, i, j) + f(8, i, j)\Delta x + f(9, i, j)(\Delta x)] \end{aligned} \quad (28)$$

The derivative representations are used to calculate the field quantities B_R and B_Z (Eqn. (1)) using the spline representation of ψ and in other places where the derivatives of the field quantities and ψ are needed.

(B) Boris-push scheme

This scheme is used to update the velocity of FK motion using the force equation in (4). The force acting on the particle consists of the electric field \mathbf{E} , which causes acceleration and changes the magnitude of \mathbf{v} , and the $\mathbf{v} \times \mathbf{B}$ force, which simply rotates the velocity vector without changing its magnitude. This allows the formulation of a physically reasonable scheme that is centred in time (with t and t' as dummy variables, $t - \Delta t/2 < t < t' < t + \Delta t/2$).

In the Lorentz force equation, the magnetic term is centred in time by averaging $\mathbf{v}_{t-\Delta t/2}$ and $\mathbf{v}_{t+\Delta t/2}$ while keeping the others unchanged. We then have

$$\frac{\mathbf{v}_{t+\Delta t/2} - \mathbf{v}_{t-\Delta t/2}}{\Delta t} = \frac{q}{m} \left[\mathbf{E} + \frac{(\mathbf{v}_{t+\Delta t/2} + \mathbf{v}_{t-\Delta t/2}) \times \mathbf{B}}{2} \right] \quad (29)$$

The method of Boris separates the electric and magnetic forces completely. We define

$$\mathbf{v}^- = \mathbf{v}_{t-\Delta t/2} + \frac{q\mathbf{E}}{m} \frac{\Delta t}{2} \quad (30)$$

$$\mathbf{v}^+ = \mathbf{v}_{t+\Delta t/2} - \frac{q\mathbf{E}}{m} \frac{\Delta t}{2} \quad (31)$$

Substituting into Eqn. (29), we get

$$\frac{\mathbf{v}^+ - \mathbf{v}^-}{\Delta t} = \frac{q}{2m}(\mathbf{v}^+ + \mathbf{v}^-) \times \mathbf{B} \quad (32)$$

We find that the electric field gets cancelled on making the substitution and we are simply left with a $\mathbf{v} \times \mathbf{B}$ rotation. The steps of computation are as follows:

(i) Add the electric impulse for the first half of the time interval to $\mathbf{v}_{t-\Delta t/2}$ to obtain \mathbf{v}^- using Eqn. (30).

(ii) Rotate \mathbf{v}^- according to Eqn. (32) to obtain \mathbf{v}^+ .

(iii) Add the electric impulse for the remainder of the time step using Eqn. (31) to obtain $\mathbf{v}_{t+\Delta t/2}$.

When the directions of \mathbf{B} and \mathbf{v} are arbitrary, a convenient method for implementing the rotation has been described by Boris.

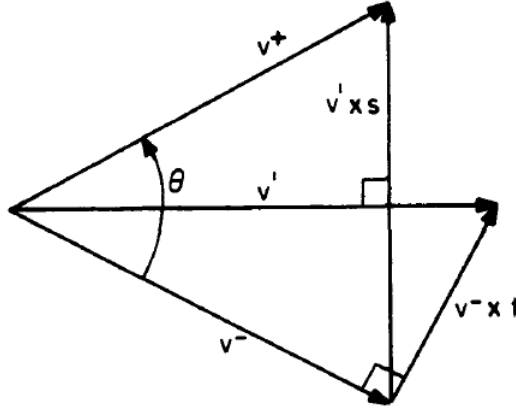


Figure 10: Velocity rotation scheme of Boris. The velocities are shown as projections of the total velocities onto the plane perpendicular to \mathbf{B} (which is assumed to be pointing into the plane). *Picture courtesy: Reference [7].*

\mathbf{v}^- is first incremented to produce a vector \mathbf{v}' which is perpendicular to both $\mathbf{v}^+ - \mathbf{v}^-$ and \mathbf{B} , as shown in Fig. 10.

$$\mathbf{v}' = \mathbf{v}^- + \mathbf{v}^- \times \mathbf{t} \quad (33)$$

The angle between \mathbf{v}^- and \mathbf{v}' is $\theta/2$ i.e. only half the rotation is done. Thus the vector \mathbf{t} is given by

$$\mathbf{t} = -\hat{\mathbf{b}} \tan \frac{\theta}{2} = \frac{q\mathbf{B} \Delta t}{m} \frac{\theta}{2} \quad (34)$$

Finally, we find that $\mathbf{v}^+ - \mathbf{v}^-$ is parallel to $\mathbf{v}' \times \mathbf{B}$, as a result of which

$$\mathbf{v}^+ = \mathbf{v}^- + \mathbf{v}' \times \mathbf{s} \quad (35)$$

\mathbf{s} is parallel to \mathbf{B} and its magnitude is determined using the fact that $|\mathbf{v}^+|^2 = |\mathbf{v}^-|^2$.

$$\mathbf{s} = \frac{2\mathbf{t}}{1 + |\mathbf{t}|^2} \quad (36)$$

Combining the above, we have in one step

$$\mathbf{v}^+ = \mathbf{v}^- + (\mathbf{v}^- \times \mathbf{s}) + [(\mathbf{v}^- \times \mathbf{t}) \times \mathbf{s}] \quad (37)$$

Since $\omega_c = qB/m$, the angle of rotation is given by

$$\theta = 2 \tan^{-1} \left(\frac{\omega_c \Delta t}{2} \right) \approx \omega_c \Delta t \left(1 - \frac{(\omega_c \Delta t)^2}{12} + \dots \right) \quad (38)$$

For a time step of $\omega_c \Delta t < 0.35$, it can be shown using the above equation that the error in θ is less than one percent.

(C) Results from the EAST tokamak

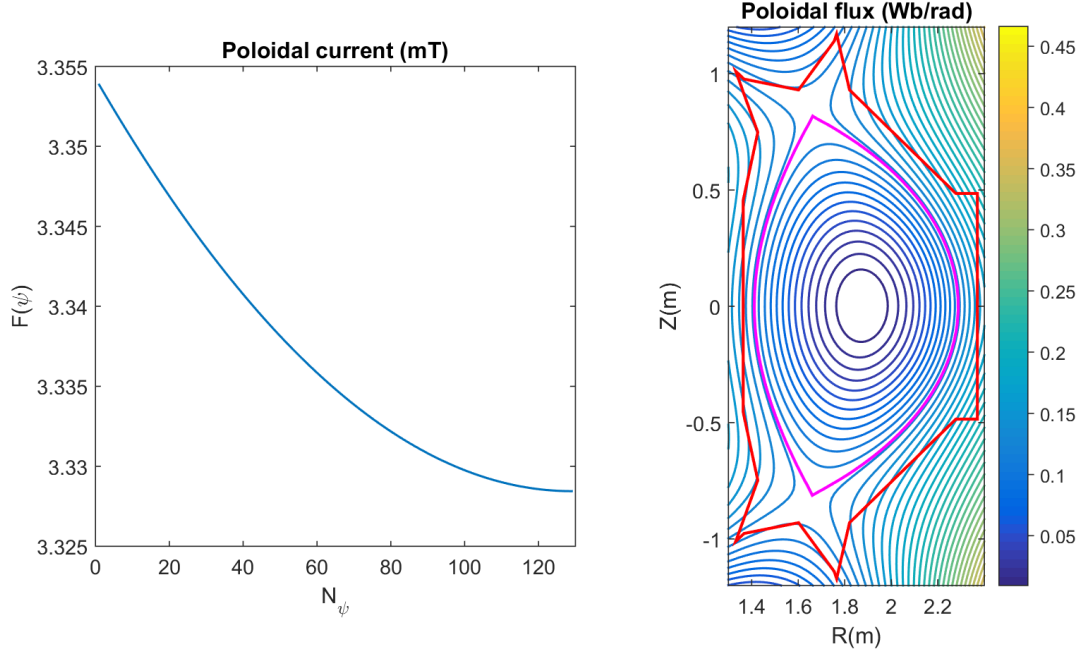


Figure 11: Poloidal current function in $m - T$ on uniform flux (left), and poloidal flux function in web/rad on rectangular (R, Z) (right) for the EAST tokamak. The magnitude of the flux function is indicated by the colours. The last closed flux surface and the limiter points are represented by the magenta and red lines, respectively.

As mentioned in the introduction, the code has also been applied to study the equilibrium of EAST which has two divertor plates, one on top and the other at the bottom of the torus. The poloidal current function and the poloidal flux are shown in Fig. 11. The magnetic field components were calculated using Eqn. (1) after constructing spline representations of $F(\psi)$ and ψ in a manner similar to what was

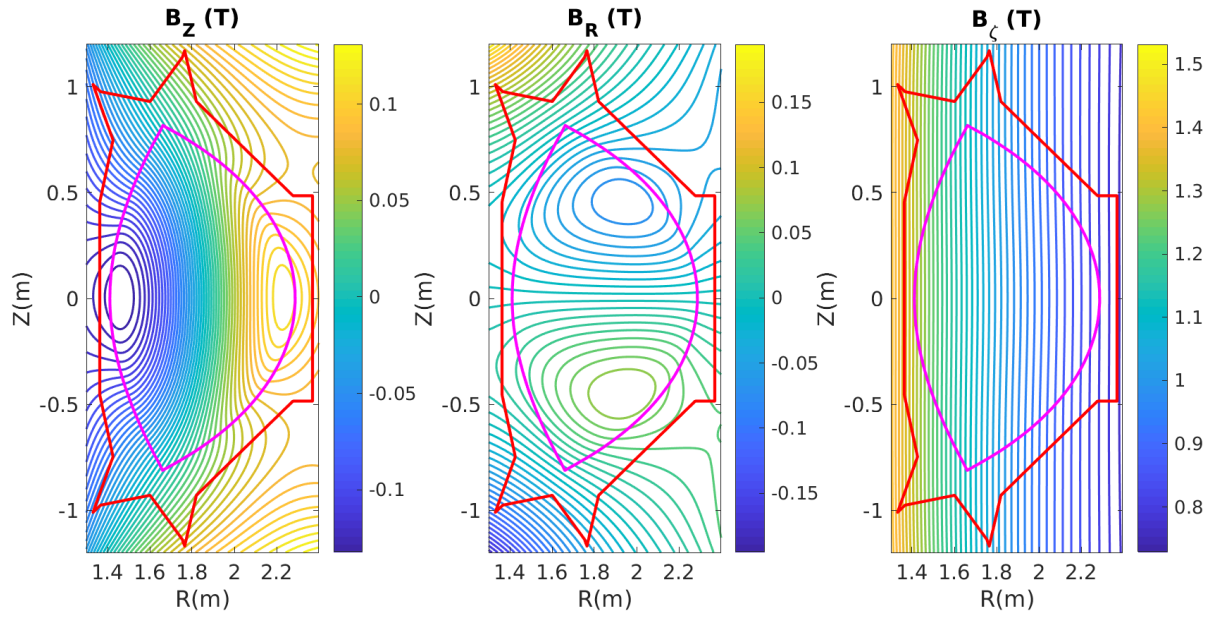


Figure 12: Contour plots of the components of the magnetic field, B_Z (left) B_R (middle) and B_ζ (right), for EAST tokamak. The magnitude of the magnetic field components are indicated by colours. The last closed flux surface and the limiter points are represented by the magenta and red lines, respectively.

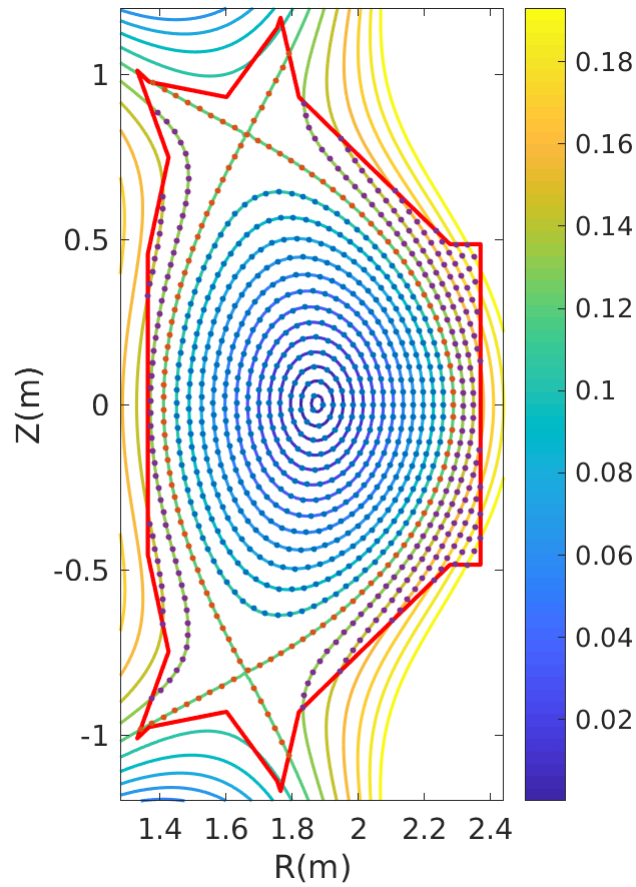


Figure 13: Field-aligned grids for the EAST tokamak. The grids in the core are shown in blue, those on the separatrix surface in red and those in the SOL region in violet. The limiter surface is drawn in red.

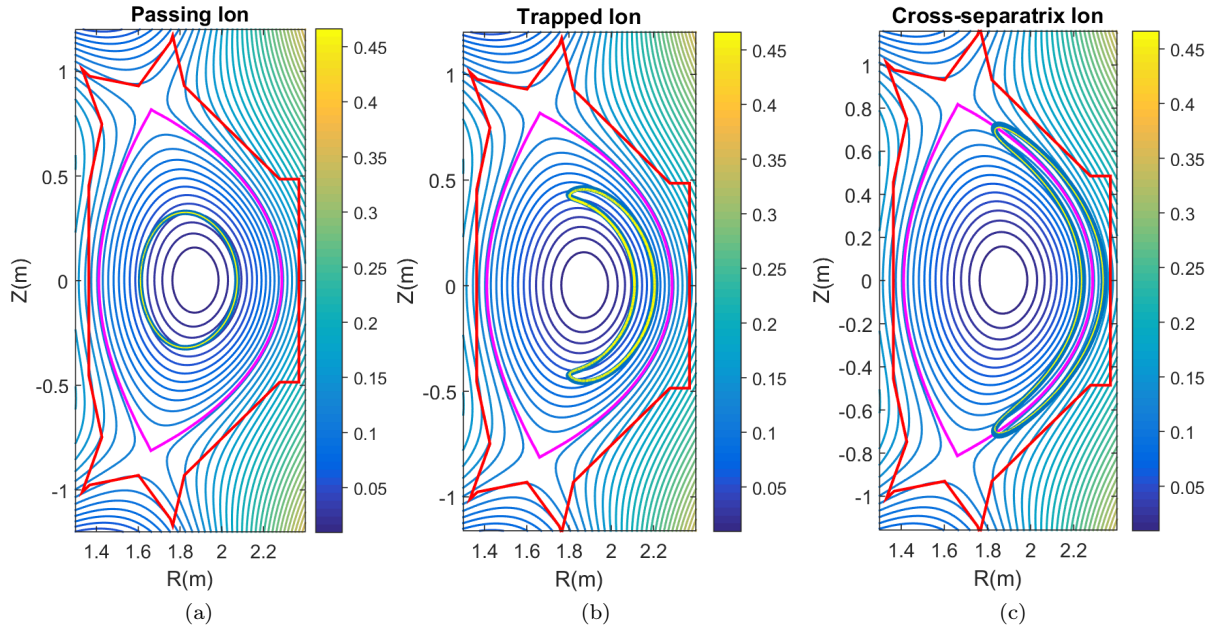


Figure 14: FK (blue) and GC(yellow) orbits of (a) a passing ion, (b) a trapped ion and (c) a cross-separatrix ion in the geometry of the EAST tokamak. The magnitude of the poloidal flux is represented by colours. The last closed flux surface and the limiter surface are shown in magenta and red respectively.

done for DIII-D tokamak. Contour plots of the field components on the poloidal cross section are shown in Fig. 12. Grid construction in this geometry is different from that in the cross section of DIII-D. The presence of two divertors causes the creation of two SOL regions, two private regions and two X-points. Hence, while constructing the grids, the two SOL regions need to be considered separately owing their discontinuity at the limiter boundary. Similarly, one needs to take into account the two X-points separately and finally merge the grids together in a cyclic manner, going in the anti-clockwise direction (following the magnetic field) along the poloidal plane. The construction of grids is shown in Fig. 13. As a final verification, we also computed the particle trajectories (both FK and GC) for passing ions, trapped ions and cross-separatrix ions in the geometry of the EAST tokamak (see Fig. 14).

References

- [1] A. Loarte, B. Lipschultz, A. S. Kukushkin, G. F. Matthews, P. C. Stangeby, N. Asakura, G. F. Counsell, G. Federici, A. Kallenbach, K. Krieger, et al., Nucl. Fusion 47, S203 (2007).
- [2] Z. Lin, T. S. Hahm, W. W. Lee, W. M. Tang, R. B. White, Science 281, 1835 (1998).
- [3] Y. Xiao, I. Holod, Z. X. Wang, Z. Lin, T. G. Zhang, Phys. Plasmas 22, 022516 (2015).
- [4] M. N. Rosenbluth, F. L. Hinton, Phys. Rev. Lett. 80, 724 (1998).
- [5] https://en.wikipedia.org/wiki/Point_in_polygon/
- [6] B. J. Sturdevant, Y. Parker, S. E. Parker, Phys. Plasmas 24, 081207 (2017).
- [7] C. K. Birdsall, A. B. Langdon, Plasma Physics via Computer Simulation (Institute of Physics, New York, 2005).
- [8] A. Brizard, T. Hahm, Rev. of Modern Phys. 79, 421 (2007).
- [9] S. De, T. Singh, A. Kuley, J. Bao, Z. Lin, G. Y. Sun, S. Sharma, A. Sen, "Kinetic particle simulations in a global toroidal geometry". Under review in *Physics of Plasmas*, AIP Publishing.